

Received August 24, 2021, accepted September 6, 2021, date of publication September 9, 2021, date of current version September 17, 2021.

Digital Object Identifier 10.1109/ACCESS.2021.3111217

Adaptive Robust Control Based on System Identification in Microgrid Considering Converter Controlled-Based Generator Modes

ISSARACHAI NGAMROO¹, (Senior Member, IEEE), AND TOSSAPORN SURINKAEW²

¹Electrical Engineering Department, School of Engineering, King Mongkut's Institute of Technology Ladkrabang, Bangkok 10520, Thailand

²School of Engineering and Technology, Central Queensland University, Perth, WA 6000, Australia

Corresponding author: Issarachai Ngamroo (mailto:issarachai.ng@kmitl.ac.th)

This work was supported by the National Research Council of Thailand.

ABSTRACT Microgrids with installation of converter controlled-based generations (CCGs), i.e. renewable energy source (RES) and battery energy storage system (BESS), may lead to a lack of system inertia. Moreover, CCG modes dominated by the CCGs may result in new control issues. Accordingly, optimal-fixed controllers designed at an operating point may not be sufficient to deal with the nonlinearity of such microgrids. This paper presents an adaptive robust control strategy of a future microgrid considering the CCG modes. Without requiring any microgrid parameters, the proposed control using a subspace-based state-space identification is used to 1) monitor microgrid changes along with moving window, 2) identify microgrid model, 3) assess stability indices, and 4) robustly design controllers of RES and BESS. Characteristic and sensitivity of the new CCG modes are analyzed. Effectiveness of the proposed control method is verified in a microgrid with 100% CCGs under various RES outputs and load patterns.

INDEX TERMS Adaptive robust control, converter controlled-based generation, low-inertia microgrid, system identification.

I. INTRODUCTION

As referred to environmental protection rules, the past few decades have witnessed a drastic growth of converter controlled-based generation (CCG), i.e. renewable energy source (RES) and battery energy storage system (BESS), especially in microgrids [1], [2]. The microgrids are able to operate in two modes, i.e. standalone or grid-connected modes [3]. In the grid-connected mode, frequency and voltage are supported by main or ideal grids, thus the problem of voltage and frequency fluctuations may not be a serious problem. However, in the standalone mode, the microgrids mainly consist of uncertain CCGs. Accordingly, the frequency and voltage fluctuations at a point of common coupling may degrade the microgrid stability. The CCGs are normally used to convert DC power from RESs and BESSs to AC loads. By means of power electronic converters, furthermore, the CCGs can regulate the voltage and maintain the microgrid stability [4]. With high penetrations of the CCGs, as they are based on power electronics, the physical inertia of the

CCGs is electrically decoupled from the microgrid networks resulting in the low-inertia or inertia-less system [5], [6]. Moreover, the control capability of CCGs may be deteriorated when it is encountered with the variability, unpredictability, and climate conditions of CCGs [7]. The general CCG controls are proposed to be embedded into the generator-tied and microgrid-tied voltage source converters while the DC bus is supported by a generator, i.e. RES or BESS. The swing equation can be applied for CCGs to determine the voltage phase angle with respect to the microgrid voltage support. As a result, the phase angle of voltage can be used to determine the voltage amplitude. Thus, to regulate the microgrid stability, the active and reactive powers of CCGs can be directly supervised by the generator-tied and microgrid-tied voltage source converters. Consequently, this scenario introduces challenging problems of future microgrid stability [7].

A problem of voltage and frequency restorations in an islanded microgrid system is addressed in [8]. A distributed secondary control scheme using decentralized finite-time approach is proposed to resolve the problem of voltage and frequency fluctuations under load variations. However,

The associate editor coordinating the review of this manuscript and approving it for publication was Nagesh Prabhu¹.

the penetration of RES is not considered. In [9], 100% CCGs using virtual synchronous generator (VSG) control are implemented in the Irish system. Two schemes, i.e. outer and inner VSGs, are considered in wind turbine generation (WTG). The results show that the frequency stability can be improved due to the fast response of the WTG. In [10], a dynamic matrix control (DMC) algorithm is applied to CCG output control in order to improve overshoot, fluctuation, and steady-state errors in the voltage and frequency responses. Nevertheless, system parameters and laborious mathematical formulations are also required to design the DMC. A frequency regulation in droop-free control for a microgrid considering electrical and communication failures is presented in [11]. It is demonstrated that the electrical and communication failures degrade the ability for confining the microgrid operation into a safe region. More detail for AC microgrid control can be found in [12], [13] and references therein. In [14], a BESS with power electronic converter is used as a VSG. A model predictive control (MPC) is applied to control BESS active and reactive outputs. The simulation and hardware-in-the-loop results show that the MPC-based BESS can support inertia during transient state and enhance the microgrid stability. Accordingly, voltage and frequency fluctuations can be suppressed. However, 1) a coordinated control with other RESs is not investigated in [11], [14], and 2) system parameters, state, input, and output matrices, are required to design the MPC proposed in [14]. In [15], the MPC and robustness optimization-based energy management system are proposed in a microgrid with RES. A supplementary Constrained Information Gap Decision Theory approach is utilized to optimize the robustness of microgrid against uncertain outputs of wind generations. In [16], an adaptive optimal MPC (AO-MPC) is applied to control a microgrid regarding weather changes, time-varying parameters, and generation unit collapse. In the simulation results, the AO-MPC provides a better control performance compared with other controllers, i.e. proportional-integral (PI), proportional-integral-derivative (PID), and optimal Fuzzy PI and PID.

Although the MPC is shown to be a better option for the microgrid control, challenges and limitations of the MPC may degrade its control performance and limit its scalability. More detail of the MPC in microgrids can be found in [17] and references therein. Besides, they require exact system parameters to design the mentioned controllers. This may not be practical in actual microgrids with uncertain CCGs, in which the microgrid parameters always change. Also, the new dominant modes introduced by CCGs are not well studied. Besides, a few works focus on the microgrids with 100% CCGs. To deal with these problems, the main contributions of this paper are highlighted as follows: 1) Analyses of the CCG modes and their impacts on the microgrid stability; 2) Applying a subspace-based state-space identification method (so-called 4SID) to design controllers of RESs and BESS without requiring any microgrid parameters; 3) Comprehensive validations in a 100% CCGs microgrid under

various loading conditions, uncertain CCG outputs, and a disconnection of CCG.

The rests of this paper are proceeded as follows: Section II describes microgrid modeling. The adaptive robust control design using subspace-based state-space identification is proposed in Section III. Performances of the proposed controller are validated in Section IV. Finally, the conclusions are made in Section V.

II. MODELING OF MICROGRID

A test microgrid system consisting of CCGs is depicted in Fig. 1. This microgrid represents 100% CCG with very low inertia. The CCGs used in this study are represented by BESS, doubly-fed induction generator (DFIG), permanent magnet synchronous generator (PMSG), and solar photovoltaic (SPV). Although microgrids with 100% CCGs have never been implemented in practice, they are expected scenarios for the near future [9], [18]. This microgrid suffers from the lack of inertia problem since the SPV is inertia-less and the inertia of DFIG and PMSG is totally decoupled from the microgrid. The virtual inertia controls as demonstrated in Fig. 2 may not be enough to regulate the microgrid stability due to highly uncertain outputs of the RESs. Accordingly, additional controllers considering crucial characteristics of the microgrid should be added to improve the microgrid stability. The nonlinear equations of system in Fig. 1 are represented by,

$$\dot{\mathbf{x}}(t) = g_x(\mathbf{x}(t), \boldsymbol{\eta} \cdot \mathbf{u}(t - \tau)), \quad (1)$$

$$\mathbf{y}(t) = g_y(\mathbf{x}(t)), \quad \exists \mathbf{y}(t) \in \mathbf{x}(t), \quad (2)$$

$$\mathbf{x} = [x_{BE}, x_{DF}, x_{PM}, x_{PV}]^T, \quad (3)$$

$$\mathbf{u} = [u_{BE}, u_{DF}, u_{PM}, u_{PV}]^T, \quad (4)$$

$$\boldsymbol{\eta} = [\eta_{BE}, \eta_{DF}, \eta_{PM}, \eta_{PV}]^T, \quad (5)$$

$$\mathbf{y} = [y_{OB}, y_{CO}]^T, \quad (6)$$

where g_x and g_y represent the nonlinear functions of state variables and outputs, t is the moving time, superscript \top is the transpose of matrix, \mathbf{x} , \mathbf{u} , and \mathbf{y} are respectively the state, input, and output vectors, $\boldsymbol{\eta} \in \{0, 1\}$ is the event-triggered logic for input \mathbf{u} , $\tau \in [0 \ 25]$ ms is the small delay caused by local measurements, subscripts BE , DF , PM , and PV mean respectively the matrices of BESS, DFIG, PMSG, and SPV, subscript OB denotes the measured signals used for the identification of microgrid, subscript CO denotes the measured signals used as the feedback of controller.

The BESS is interfaced to the microgrid via voltage source inverter (VSI). In this paper, active and reactive powers supported by BESS are controlled by VSI. A 5th-order model is considered for the BESS [19]. Accordingly, control vectors in the VSI are regarded as the state variables of BESS as given by: $x_{BE} = [v_{BE}^{dc}, i_{BE}^d, i_{BE}^q, v_{BE}^d, v_{BE}^q]$, where v and i are the voltage and current, superscripts d and q represent the direct and quadrature reference axes, and superscript dc means the DC link.

The DFIG is modelled by a 7th-order model consisting of dynamics from: 1) rotor angular speed of DFIG, 2) $d - q$

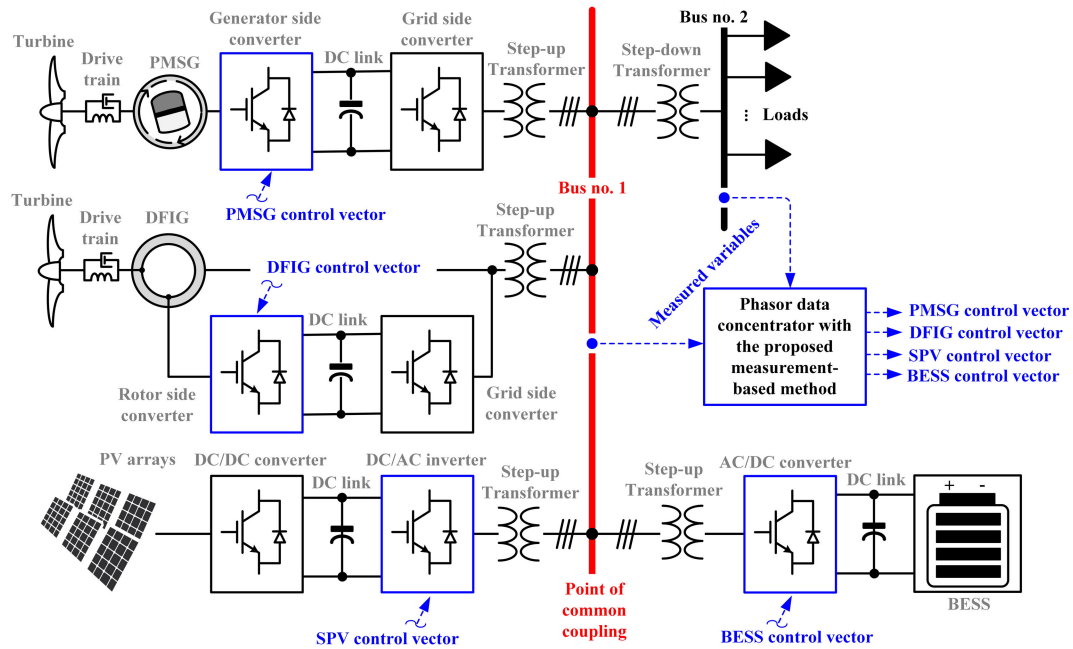


FIGURE 1. Test microgrid system.

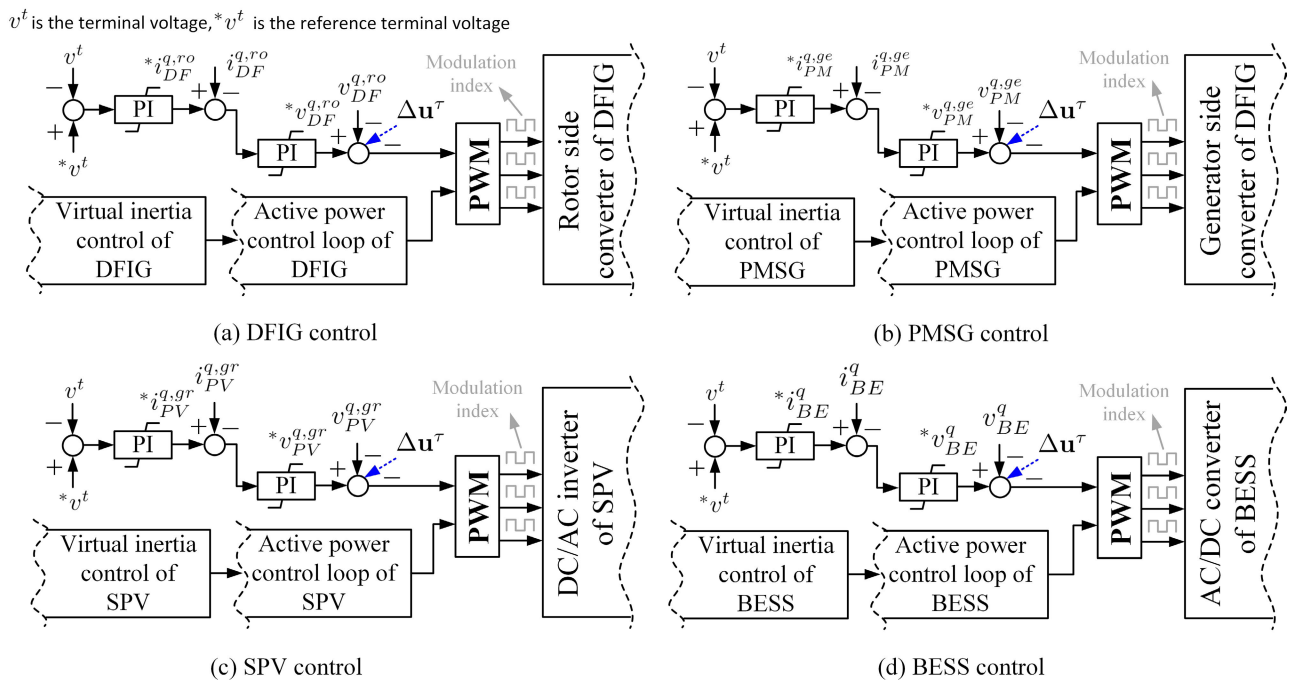


FIGURE 2. Control strategies of DFIG, PMSG, SPV, and BESS.

axis currents of rotor and grid side converters, 3) voltage of DC link, and 4) pitch angle [20]. Similarly, the PMSG is also modelled by a 7th-order model comprising dynamics from: 1) rotor angular speed of PMSG, 2) $d - q$ axis currents of generator and grid side converters, 3) voltage of DC link, and 4) pitch angle [21]. The DFIG and PMSG are

connected to the microgrid via voltage source converters. By means of the converter, the DFIG and PMSG are able to independently control the active and reactive powers injected into the microgrid. The state variables of DFIG and PMSG are given by, $x_{DF} = [\omega_{DF}, v_{DF}^{dc}, i_{DF}^{d,ro}, i_{DF}^{q,ro}, i_{DF}^{d,gr}, i_{DF}^{q,gr}, \theta_{DF}]$,

$x_{PM} = [\omega_{PM}, v_{PM}^{dc}, i_{PM}^{d,ge}, i_{PM}^{q,ge}, i_{PM}^{d,gr}, i_{PM}^{q,gr}, \theta_{PM}]$, where ω is the rotor angular speed, θ is the pitch angle, superscripts *ro* and *gr* denote rotor- and grid-side converters, and superscript *ge* means the generator-side converter.

The dynamic behavior of SPV is dominated by the converters and associated controls, i.e. active (or power factor), and reactive power (or voltage) controls. The SPV is modelled by a 7th-order model including dynamics from: 1) SPV current, 2) inductor current of DC-DC converter, 3) DC link voltage, and 4) $d - q$ axis currents and voltages of DC-AC converter [22]. The state variables of SPV are given by: $x_{PV} = [i_{PV}, i_{PV}^l, v_{PV}^{dc}, v_{PV}^{d,gr}, v_{PV}^{q,gr}, i_{PV}^{d,gr}, i_{PV}^{q,gr}]$, where superscript *l* denotes the inductor.

It should be noted that the differential equations of these state variables are provided in Appendix. In this paper, new modes in the microgrid originated by CCGs are defined as ‘‘CCG modes’’. These CCGs may cause new issues regarding microgrid operation and control as follows:

- 1) The CCGs may create new CCG modes completely associated with the CCG state variables. Typical control methods may be ineffective since these CCG modes may not be sensitive to conventional controllers. The CCG modes occurred in low-inertia microgrid with 100% CCGs may be more detrimental to the system with higher inertia.
- 2) Drastic changes in the CCG uncertain outputs may make the microgrid more unpredictable and harder to monitor and control;
- 3) Three major mechanisms by which they can affect the new CCG modes are i) displacing conventional machines that have well-tuned controllers, ii) impacts of uncertain power flows, and iii) CCG controls interacting with such new CCG modes.

To analyze the CCG modes, the linearization of microgrid in a small time range (Δt) is represented by the state equation as follows:

$$\dot{\mathbf{x}}(\Delta t) = \mathbf{A}\mathbf{x}(\Delta t) + \mathbf{B}\boldsymbol{\eta} \cdot \mathbf{u}(\Delta t - \tau), \quad (7a)$$

$$\Delta \dot{\mathbf{x}} = \mathbf{A}\Delta \mathbf{x} + \sum_{n_{cg}=1}^{N_{cg}} \left(\eta_{n_{cg}} \mathbf{B}_{n_{cg}} \mathbf{u}_{n_{cg}}^\tau \right), \quad (7b)$$

$$\mathbf{y}(\Delta t) = \mathbf{C}\mathbf{x}(\Delta t), \quad (8a)$$

$$[\Delta y_{OB} \ \Delta y_{CO}]^T = [\mathbf{C}_{OB} \ \mathbf{C}_{CO}]^T \Delta \mathbf{x}, \quad (8b)$$

where Δ means the small variation, \mathbf{u}^τ is the input vector including a small delay, \mathbf{A} , \mathbf{B} , \mathbf{C} are respectively the state, input, and output matrices, $n_{cg} = 1, \dots, N_{cg}$ is the counter of corresponding converter controlled-based generation, and N_{cg} is the total number of converter controlled-based generations.

To avoid the degradation of active power supported into the microgrid, the additional signal $\Delta \mathbf{u}^\tau$ is injected into the reactive power control loops of DFIG, PMSG, SPV, and BESS. Moreover, the inertia emulation control techniques are applied in active power control loops of CCGs in order

to support an inertial response to the microgrid. However, the inertia emulation control techniques are not focused in this study since the additional signal $\Delta \mathbf{u}^\tau$ is not injected into this loop. Numerous virtual inertia control strategies, which are applied for CCGs can be found in [2]. Fig. 2 demonstrates the control strategies of DFIG, PMSG, SPV, and BESS.

Rewriting the input vector in (7b) in the form of controller \mathbf{k} , yields $\Delta \mathbf{u}^\tau = -\mathbf{k}\Delta y_{CO}$. Next, let $\Delta \mathbf{u}^\tau = [\Delta u_1^\tau, \dots, \Delta u_{N_{cg}}^\tau]$, substituting $\Delta y_{CO} = \mathbf{C}_{CO}\Delta \mathbf{x}$ in (7c) into (7c) obtains,

$$\Delta \mathbf{u}^\tau = -\mathbf{k}(\mathbf{C}_{CO}\Delta \mathbf{x}) \quad (9a)$$

$$\begin{aligned} [\Delta u_1^\tau, \dots, \Delta u_{N_{cg}}^\tau]^\top &= -[\mathbf{k}(\mathbf{C}_{CO,1}\Delta \mathbf{x}), \dots \\ &\dots, \mathbf{k}(\mathbf{C}_{CO,N_{cg}}\Delta \mathbf{x})]^\top. \end{aligned} \quad (9b)$$

In this paper, the controller \mathbf{k} is the low-order fixed structure controller. Accordingly, the controller \mathbf{k} can be written by the transfer function,

$$\mathbf{k}(s) = \frac{x_p^k + x_{p-1}^k s^{-1} + \dots + x_1^k s^{1-p} + x_0^k s^{-p}}{1 + y_{q-1}^k s^{-1} + \dots + y_1^k s^{1-q} + y_0^k s^{-q}}, \quad (10)$$

where s is the complex number, $x_p^k, x_{p-1}^k, \dots, x_0^k$ are the numerator parameters, and $y_q^k, y_{q-1}^k, \dots, y_0^k$ are the denominator parameters. It should be noted that values of p and q can be specified by the designers so that the small order of \mathbf{k} can be appropriately chosen.

The design of \mathbf{k} will be given in Sections III-B and III-C. Accordingly, the closed-loop state equation including controller (\mathbf{x}_{cl}) is derived by substituting (9b) into (7b) as $\Delta \dot{\mathbf{x}}_{cl} = \mathbf{A}_{cl}\Delta \mathbf{x}_{cl}$, where $\mathbf{A}_{cl} = \mathbf{A} - \sum_{n_{cg}=1}^{N_{cg}} (\eta_{n_{cg}} \mathbf{B}_{n_{cg}} \mathbf{k}_{CO,n_{cg}})$, $\mathbf{A}_{cl} \in \mathbb{R}^{n_{cl} \times n_{cl}}$ is the closed-loop state matrix, and n_{cl} is the total number of closed-loop state variables. However, the matrix \mathbf{A}_{cl} can be obtained when all of the microgrid parameters are exactly known. In uncertain microgrids, these parameters are obscured and may be varied according to the microgrid operating point and topology. Thus, it is difficult to investigate the microgrid stability by calculating \mathbf{A}_{cl} . To estimate the linearized matrix elements without requiring any microgrid parameters, an identification method is proposed in the next section.

III. ADAPTIVE ROBUST CONTROL DESIGN USING SUBSPACE-BASED STATE-SPACE IDENTIFICATION

A. SUBSPACE-BASED STATE-SPACE SYSTEM IDENTIFICATION

In this paper, the 4SID is applied to estimate the closed-loop system model without requiring any microgrid parameters [23], [24]. The 4SID requires signals from measurements or observations from the system for a black-box identification. This approach is done by formulating the identification problem as an optimization problem, in which the variables are the unknown parameters of the model. The constraints are the model equations while the objective function is a measure of the deviation between the observations and the

predictions (or simulations) obtained from the model [25]. Since the 4SID is well studied in previous research works, more details of the fitting functions related to the 4SID can be found in Appendix. Accordingly, a system including the CCG modes can be estimated by the system identification technique. The 4SID of the microgrid in Fig. 1 is written by,

$$f_{si}(SI_i, SI_o) = [\hat{A}, \hat{B}, \hat{C}, \hat{D}], \quad (11a)$$

$$\text{Subject to: } \sigma < \sigma^*, t_c < \epsilon \Delta t, ac > 90\%, \\ n_c < \lfloor 0.5 \text{ length}(\mathbf{x}) \rfloor, \quad (11b)$$

where f_{si} represents the function of system identification using subspace-based method (for more detail, see Appendix), SI_i is the microgrid input, which can trigger the CCG modes, SI_o is the microgrid output, which can observe the response of the CCG modes, both SI_i and SI_o are obtained by measurements in microgrid, when $\{SI_i, SI_o\} \in \Delta y_{OB}$, and they are used as the inputs of f_{si} , and \hat{A} , \hat{B} , \hat{C} and \hat{D} are respectively the estimated state, input, output, and feed-forward matrices, length means the length of matrix, σ and σ^* are respectively the actual and desired singular values, t_c is the computational time of (11a), $\epsilon \in (0.1 \ 0.5)$ is the factor, which is used to make sure that t_c is five to ten times lesser than Δt , ac is the accuracy of estimated model, $\lfloor \cdot \rfloor$ means the greatest integer which is less than or equal to its argument, and $n_c \in \mathbb{Z}$ is the order of estimated state matrix \hat{A} .

In this paper, ac is calculated by the mean error of the corresponding data deviation as: $ac = \left(1 - \sum_{n_d=1}^{n_{id}} \left| \frac{S_{n_d}^L - S_{n_d}^F}{S_{n_d}^F} \right| / n_{id} \right) \times 100$, where subscript $n_d = 1, \dots, n_{id}$ is the data index and S^L and S^F are the data obtained from the estimated and full models, respectively.

Equation (11b) is used to guarantee 1) containing crucial features of the original model, 2) small computational time, 3) high accuracy of the estimated model, and 4) low order of the estimated model (less than half of the original model). Hence, the variable SI_i is obtained by: $SI_i = \Delta \bar{P} = \frac{\Delta P_{DF} + \Delta P_{PM} + \Delta P_{PV} + \Delta P_{BE} + \sum_{l=1}^{N_l} (\Delta P_{L,l})}{4 + N_l}$, and the variable SI_o is obtained by: $SI_o = \Delta F$, where ΔP_{DF} , ΔP_{PM} , ΔP_{PV} , and ΔP_{BE} are respectively the power deviations of DFIG, PMSG, SPV, and BESS, $\Delta P_{L,l}$ is the load variation, subscript $l = 1, \dots, N_l$ is the counter of loads, N_l is the total number of loads, and ΔF is the frequency deviation. It should be noted that the signal SI_i is the average value of the measured signals ΔP_{DF} , ΔP_{PM} , ΔP_{PV} , ΔP_{BE} , and $\Delta P_{L,l}$. These signals contain crucial features of the corresponding CCG modes (i.e. damping and frequency). Note that the justification of signal SI_i will be demonstrated in Section IV-A.

The changes in such signals can trigger observable responses of the CCG modes. The characteristic of ΔF can be represented by the form of the CCG modes as: $\Delta F = \sum_{m=1}^{n_{cl}} \Delta S_m \cos(2\pi f_m \Delta t) e^{-\zeta_{cl,m} \Delta t}$, where e is the exponential constant, $m = 1, \dots, n_{cl}$ is the number of corresponding CCG mode, S_m is the amplitude of response caused by the m^{th} CCG modes, f_m and $\zeta_{cl,m}$ are the frequency and damping ratio of the m^{th} CCG mode, respectively.

During the changes in microgrid, the signal ΔF contains characteristics of modes and it is obtained by local measurements with time stamp in the range of 40 to 100 ms. By using (11a) to estimate the microgrid model, the signal ΔF is dominated by $\zeta_{cl,m}$. It can be seen that the higher the value of $\zeta_{cl,m}$, the lower the value of ΔS_m .

After adding the signal $\Delta \mathbf{u}^T$, the estimated closed-loop state matrix of microgrid (\hat{A}_{cl}) can be calculated by,

$$\hat{A}_{cl} = \hat{A} - \hat{B} \mathbf{k} \hat{C}. \quad (12)$$

In (12), the matrix \hat{A}_{cl} is calculated by \hat{A} , \hat{B} , and \hat{C} , which are estimated by (11a) with the constraints in (11b). Thus, any exact system parameters are not required to formulate the state-space model of microgrids. This is the main advantage of the proposed 4SID to conduct the steady state solution. Accordingly, the matrix \hat{A}_{cl} with high accuracy of the estimation can be used to calculate the stability indices such as eigenvalue, damping ratio, and system robustness, described as follows: Eigenvalues and damping ratios of the estimated microgrid model including the CCG modes can be calculated by: $\det(\hat{A}_{cl} - \hat{\lambda}_{cl} I) = 0$, $\hat{\lambda}_{cl} = [\hat{\sigma}_1 \pm j2\pi \hat{f}_1, \dots, \hat{\sigma}_{n_{cl}} \pm j2\pi \hat{f}_{n_{cl}}]$, and $\hat{\zeta}_{cl} = [\frac{-\hat{\sigma}_1}{\sqrt{\hat{\sigma}_1^2 + (2\pi \hat{f}_1)^2}}, \dots, \frac{-\hat{\sigma}_{n_{cl}}}{\sqrt{\hat{\sigma}_{n_{cl}}^2 + (2\pi \hat{f}_{n_{cl}})^2}}]$, where det denotes the determinant of matrix, subscript $cl = 1, \dots, n_{cl}$ means the counter of the CCG modes, n_{cl} is the total number of the CCG modes, $I \in \mathbb{R}^{n_{cl} \times n_{cl}}$ is the identity matrix, $\hat{\lambda}_{cl}$ and $\hat{\zeta}_{cl}$ are the vectors of the estimated eigenvalue and damping ratio, $j = \sqrt{-1}$ is the complex number, $\hat{\sigma}$ is the estimated real part, and \hat{f} is the estimated frequency.

To observe the CCG modes, the small time range (Δt) in (7a) is set by,

$$\Delta t \in \left[\left(\max(\hat{f}_1, \dots, \hat{f}_{n_{cl}}) \right)^{-1} \left(\min(\hat{f}_1, \dots, \hat{f}_{n_{cl}}) \right)^{-1} \right], \quad (13)$$

where min and max represent the minimum and maximum values.

Note that (13) is used to make sure that i) the highest frequency of the CCG modes can be observed, and ii) the time range Δt used for the estimation of the CCG modes is selected properly.

B. CONTROLLER DESIGN

The robustness indices calculated by the estimated matrices \hat{A} , \hat{B} , \hat{C} , and \hat{D} are described in this section. It is well known that each robust control method is mainly useful for capturing a set of design specification. For instance, the H_2 tracking control is suitable to deal with transient performance by minimizing the linear quadratic cost of tracking error and control output, while H_∞ approach is more useful to maintain the closed-loop stability in the presence of model uncertainties [26]. Besides, the damping of the CCG modes is kept greater than or equal to an acceptable value so that the ability to recover microgrid responses to a steady state

can be achieved after disturbances. Accordingly, as presented in Fig. 3, a mixed H_2/H_∞ control technique [27], [28] considering damping of the CCG modes can satisfy such objectives, where \hat{G} is the nominal plant, which is equivalent to $\begin{bmatrix} \hat{A} & \hat{B} \\ \hat{C} & \hat{D} \end{bmatrix}$, w_∞ and y_∞ are the input and output of microgrid related to Δ_M , Δ_M is the sensitivity functions which are related to possible uncertainties in the microgrid, and w_2 and y_2 are the input and output of microgrid related to the linear quadratic cost of tracking error and control output. The proofs of Δ_M are given in Appendix.

A mixed H_2/H_∞ of a static output feedback control design can be achieved by minimizing the following optimization problem (J) as,

$$\text{Minimize: } J = \alpha_1 \|T_{y_\infty w_\infty}\|_\infty + \alpha_2 \|T_{y_2 w_2}\|_2, \quad (14a)$$

$$\text{Subject to: } \hat{\xi}_{cl} > \hat{\xi}_{cl}^*, \|T_{y_\infty w_\infty}\|_\infty' < \varepsilon_1, \\ \|T_{y_2 w_2}\|_2' < \varepsilon_2, \quad (14b)$$

$$\text{when: } \|T_{y_\infty w_\infty}\|_\infty' = \left| \|T_{y_\infty w_\infty}\|_\infty - \|T_{y_\infty w_\infty}\|_\infty^* \right|, \\ \|T_{y_2 w_2}\|_2' = \left| \|T_{y_2 w_2}\|_2 - \|T_{y_2 w_2}\|_2^* \right|, \quad (14c)$$

where $\|\cdot\|_\infty$ and $\|\cdot\|_2$ mean the ∞ -norm and 2-norm, α_1 and α_2 are the weighting factors of the first and second terms of (14a), $\hat{\xi}_{cl}^* = \{\hat{\xi}_{cl,1}^*, \dots, \hat{\xi}_{cl,n_{cl}}^*\}$ is the vector of the desired damping ratio of $\hat{\xi}_{cl}$, when $\hat{\xi}_{cl,1}^*, \dots, \hat{\xi}_{cl,n_{cl}}^*$ are respectively the specified values of $\hat{\xi}_{cl,1}, \dots, \hat{\xi}_{cl,n_{cl}}$, $T_{y_\infty w_\infty}$ is the transfer function between y_∞ and w_∞ , $\|T_{y_\infty w_\infty}\|_\infty$ is the absolute difference between $\|T_{y_\infty w_\infty}\|_\infty$ and $\|T_{y_\infty w_\infty}\|_\infty^*$, $\|T_{y_\infty w_\infty}\|_\infty^*$ is the desired value of $\|T_{y_\infty w_\infty}\|_\infty$, $\|T_{y_2 w_2}\|_2'$ is the absolute difference between $\|T_{y_2 w_2}\|_2$ and $\|T_{y_2 w_2}\|_2^*$, when $\|T_{y_2 w_2}\|_2^*$ is the desired value of $\|T_{y_2 w_2}\|_2$, and ε_1 and ε_2 are the small real positive numbers set by designers.

Values of $T_{y_\infty w_\infty}$ and $T_{y_2 w_2}$ are obtained by [29]: $T_{y_\infty w_\infty} = [\Delta_{M1}, \Delta_{M2}, \Delta_{M3}]$, $\Delta_{M1} = (I + \hat{G}k)^{-1}$, $\Delta_{M2} = -(I + \hat{G}k)^{-1} \hat{G}k$, $\Delta_{M3} = k(I + \hat{G}k)^{-1}$, and $T_{y_2 w_2} = |r - \Delta_{yCO}|$, where Δ_{M1} is the sensitivity function used to evaluate the disturbance attenuation level, Δ_{M2} is the sensitivity function used for noise rejection in measurements, Δ_{M3} is the sensitivity function used to reduce the energy effort of controller k , $|\cdot|$ means the absolute value, and r is the reference signal. However, the objective function (14a) can deal with uncertainties in limited operations around the designed operating point. As a result, an adaptive robust control algorithm is required in low-inertia microgrids with CCGs.

C. PROPOSED CONTROL CONSIDERING CCG MODES

The proposed control considering the CCG modes is applied to adjust control parameters in k according to the changes in microgrid operating points. Let subscript a represents the a^{th} operating point, the change in microgrid operating point is written by: $\hat{G}_{a+1} = \hat{G}_a \pm \Delta\hat{G}$. Accordingly, the change $\Delta\hat{G}$ leads to the changes in the microgrid stability indices

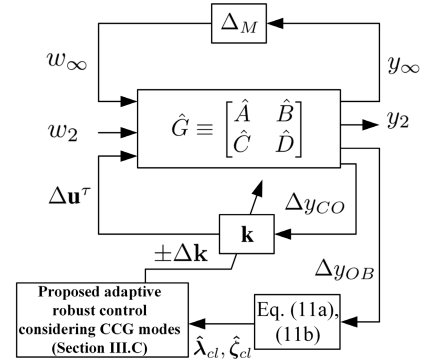


FIGURE 3. Mixed H_2/H_∞ considering CCG modes.

as follows: $\hat{\lambda}_{cl,a+1} = \hat{\lambda}_{cl,a} \pm \Delta\hat{\lambda}_{cl}$, $\hat{\xi}_{cl,a+1} = \hat{\xi}_{cl,a} \pm \Delta\hat{\xi}_{cl}$, $\|T_{y_\infty w_\infty}\|_{\infty,a+1} = \|T_{y_\infty w_\infty}\|_{\infty,a} \pm \Delta\|T_{y_\infty w_\infty}\|_\infty$ and $\|T_{y_2 w_2}\|_{2,a+1} = \|T_{y_2 w_2}\|_{2,a} \pm \Delta\|T_{y_2 w_2}\|_2$.

In weak microgrids with 100% CCGs, a small change in $\Delta\hat{G}$ may lead to significant changes in the microgrid stability, i.e. $\Delta\hat{\lambda}_{cl}$ and $\Delta\hat{\xi}_{cl}$. If $\hat{\xi}_{cl,a+1} < \hat{\xi}_{cl,a}$ and $\hat{\xi}_{cl,a+1} < \hat{\xi}_{cl}^*$, the designed k is used to move $\hat{\xi}_{cl,a+1}$ to the value which is greater than the acceptable value, i.e. $\hat{\xi}_{cl,a+1} \geq \hat{\xi}_{cl}^*$. If $\|T_{y_\infty w_\infty}\|_{\infty,a+1} < \|T_{y_\infty w_\infty}\|_{\infty,a}$ and $\|T_{y_\infty w_\infty}\|_{\infty,a+1} > \varepsilon_1$, the designed k is utilized to minimize the value of $\|T_{y_\infty w_\infty}\|_{\infty,a+1}$ and make sure that $\|T_{y_\infty w_\infty}\|_{\infty,a+1} < \varepsilon_1$. If $\|T_{y_2 w_2}\|_{2,a+1} < \|T_{y_2 w_2}\|_{2,a}$ and $\|T_{y_2 w_2}\|_{2,a+1} > \varepsilon_2$, in the same way, the designed k is utilized to minimize the value of $\|T_{y_2 w_2}\|_{2,a+1}$ and make sure that $\|T_{y_2 w_2}\|_{2,a+1} < \varepsilon_2$. Based on these concepts, the proposed adaptive robust control considering the CCG modes is illustrated by the flowchart in Fig. 4.

IV. PERFORMANCE EVALUATION

In this section, the simulation study is divided into three parts, i.e. model validation, analysis of the CCG modes, and time-domain simulation. The effectiveness of the proposed k is investigated in the microgrid depicted in Fig. 1. The microgrid base is set at 1 MW 50 Hz, loads are assumed to be varied between 1.5 and 4.5 MW. Accordingly, the DFIG, PMSG, and SPV are operated between 0.25 and 1.5, 0.25 and 1.5, and 0.25 and 1 MW respectively. It is assumed that the BESS is ideal and enough to manage uncertain outputs from the RESs and loads.

A. MODEL VALIDATION

Effectiveness of using different input signals SI_i under various scenarios is justified. The simulation environment is conducted at the normal operating point when the controllers are not installed. It is assumed that the loads, wind speed, and solar irradiation are fluctuated. Fig. 5 shows microgrid responses when SI_i is the mean active power output deviation ($\Delta\bar{P}$), mean reactive power output deviation ($\Delta\bar{Q} = \frac{\Delta Q_{DF} + \Delta Q_{PM} + \Delta Q_{PV} + \Delta Q_{BE} + \sum_{l=1}^{N_l} (\Delta Q_{L,l})}{4+N_l}$), or voltage deviation at bus 1 ($\Delta V_1 = 1 - V_1$). As can be seen, when $SI_i = \Delta\bar{P}$,

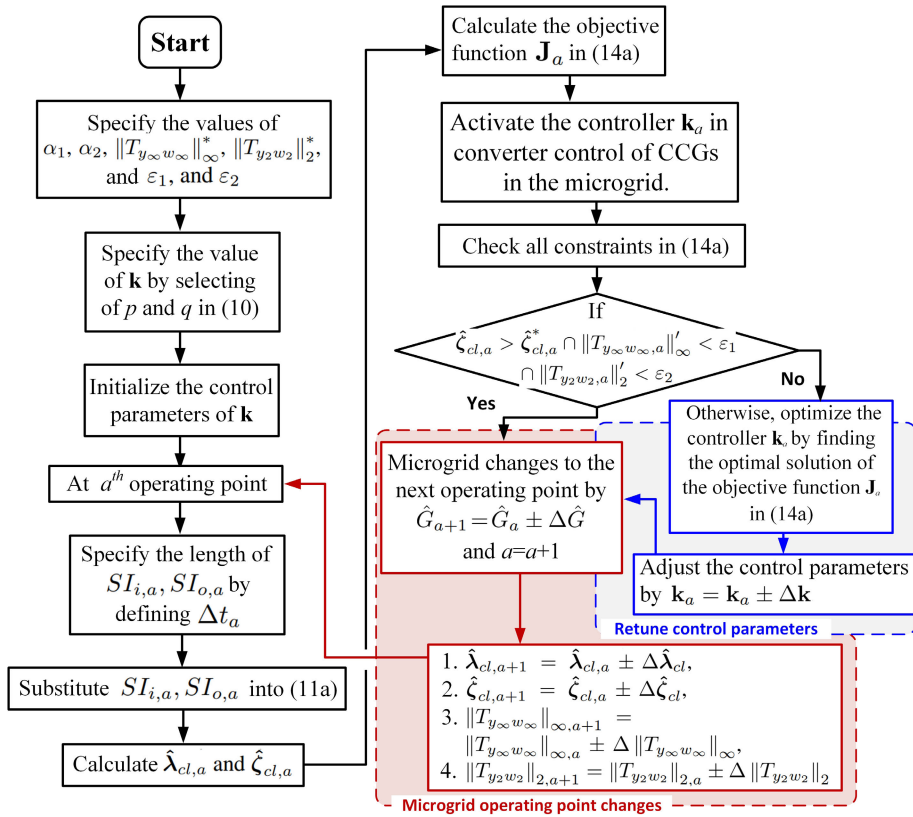


FIGURE 4. Flowchart of the proposed control algorithm.

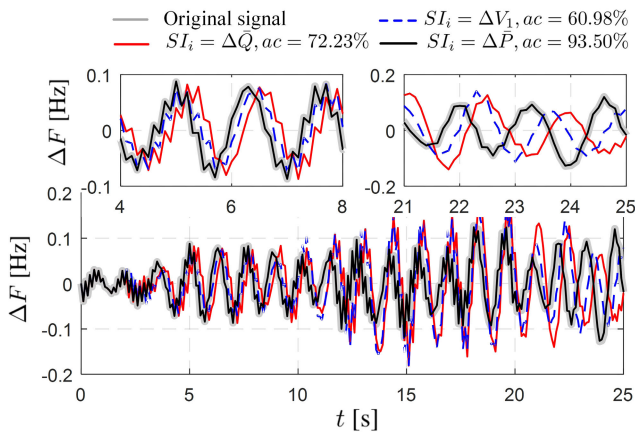


FIGURE 5. Microgrid responses estimated by 4SID under different inputs SI_i .

it provides the highest accuracy ac . Moreover, 500 different scenarios are also conducted with the same criteria when the generations of RESs and loads are randomly changed by $\pm 20\%$, for the active power, and $\pm 5\%$, for the reactive power. As a result, the values of ac vary between 90.50 and 96.62%, for $SI_i = \Delta \bar{P}$, 62.72 and 85.11%, for $SI_i = \Delta \bar{Q}$, and 35.10 and 70.78%, for $SI_i = \Delta V_1$. Accordingly, signal $\Delta \bar{P}$ is the most suitable candidate for using as the input of 4SID.

The estimated model is also verified by comparison with the full model. The estimated model is obtained by (11a)

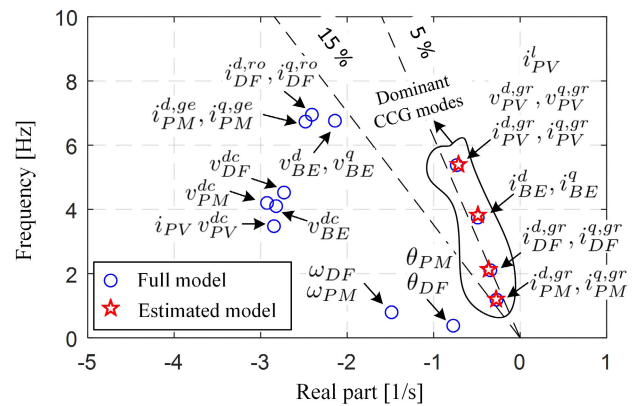


FIGURE 6. Eigenvalue analysis result of full and estimated models.

while the full model is created by the state-space model of the differential equations of DFIG, PMSG, SPV, and BESS given in Appendix. Fig. 6 demonstrates eigenvalue analysis result of full and estimated models. For the full model, the participation factor is used to differentiate the association of each state variable and eigenvalue. It can be seen that the locations of eigenvalues with 5 to 15% damping ratio (dominant modes) are identical. In this microgrid, the eigenvalues with greater than 15% damping ratio are well damped and they do not create any stability issues. Obviously, the proposed 4SID can capture the oscillation frequencies and

amplitudes of dominant modes. Consequently, the low-order estimated model, which is obtained by the 4SID, contains crucial features of such dominant modes. This verifies that the estimated model is sufficient to design the controller \mathbf{k} . It should be noted that, without requiring any exact microgrid parameters, the participation of eigenvalues obtained by the 4SID is justified in the next section.

B. ANALYSIS OF CCG MODES

Characteristics of the CCG modes (i.e. damping, frequency, and participation) are analyzed in this section. To individually analyze the CCG modes, either P_{DF} , P_{PM} , P_{PV} , or P_{BE} is varied while the others are fixed as constant values. To identify the CCG modes, the controller \mathbf{k} is not installed in the CCGs. Fig. 7 shows the input and output pairs used for identification of CCG mode using 4SID. Accordingly, Fig. 8 demonstrates the analysis results of the CCG mode. In Figs. 7(a) and (b), the active power of DFIG P_{DF} is assumed to be varied while P_{PM} , P_{PV} , P_{BE} , and $\Delta P_{L,i}$ are fixed as constant values, then the output ΔF is observed to conduct the CCG mode analysis. The settings of 4SID in (11a) and (11b) are decided as follows: the order of estimated model is set by $n_c = 8$ (the order of microgrid is 26), the desired singular value is set by $\sigma^* = 10^{-5}$, and the observed time is set by $\Delta t = 1$ s. At the accuracy of estimated model $ac > 90\%$, the computational time t_c is varied between 7 and 25 ms. Consequently, Figs. 8(a) and (b) show the estimated damping ratios and frequencies of the CCG modes. As can be observed, there are four dominant modes, those damping ratios are lower than 0.2 (or 20%). However, the frequencies are almost constant at approximately 1.78, 2.21, 3.32, and 5.02 Hz. To define the participation of each CCG mode, the variance of the

estimated damping ratio ($v^2 = \frac{\sum_{r=1}^{n_r} (\hat{\xi}_r - \bar{\xi})^2}{n_r}$), where $\bar{\xi}$ is the mean value of $\hat{\xi}_r$, $r = 1, \dots, n_r$, and $n_r = \frac{120}{6}$ is the total number of estimated $\hat{\xi}_r$ data within the simulation time, is applied to track the variations of $\hat{\xi}_r$ and ΔP_{DF} . As a result, the values of v^2 are 2.19, 0.14, 0.82, and 0.11 for the 1st, 2nd, 3rd, and 4th CCG modes, respectively. As can be seen, the 1st CCG mode (blue-dashed line) provides the greatest value of v^2 . The variation of ΔP_{DF} leads to a major change in the damping ratio of the 1st CCG mode. This implies that the 1st CCG mode belongs to the DFIG.

Same criteria is also applied to estimate the other CCG modes with different pairs of SI_i and SI_o (see Figs. 7 (c)-(h) and Figs. 8 (c)-(h)). It can be summarized that the 2nd, 3rd, and 4th CCG modes belong to the PMSG, SPV, and BESS, respectively.

C. TIME-DOMAIN SIMULATION

The time-domain simulation is conducted to verify effectiveness of the proposed \mathbf{k} . The proposed controller is referred to as \mathbf{k}_p , where $\mathbf{k}_a \in \mathbf{k}_p$. As can be seen in Fig. 6, there are four dominant CCG modes. To effectively improve these modes, the order of controller should be more than or equal to 8th order. Accordingly, the 8th-order controller is selected.

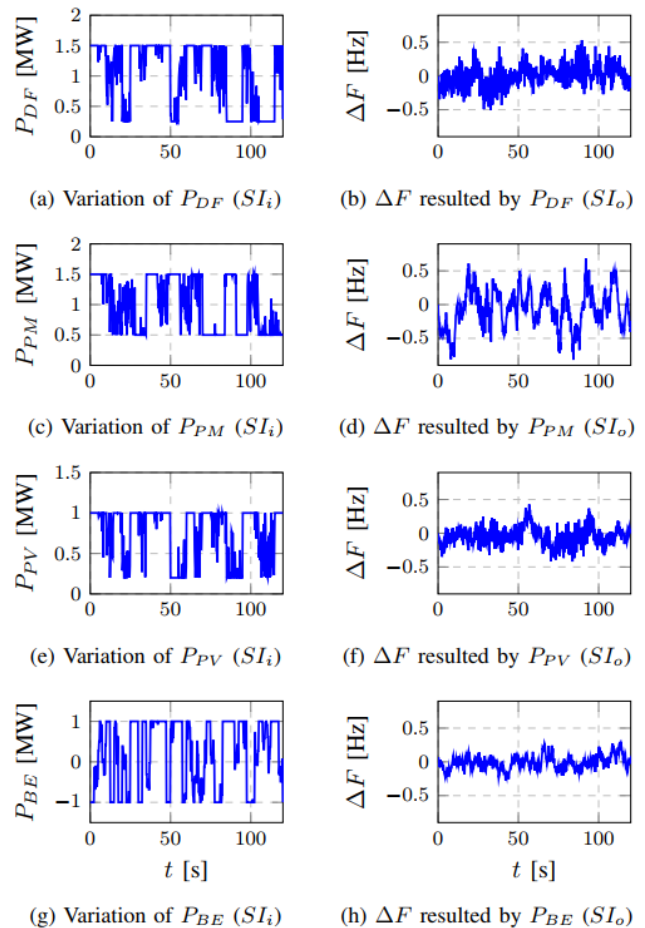


FIGURE 7. Input SI_i and output SI_o used for analysis of CCG modes.

It should be noted in (10) that, when $p = q = 8$, this selection represents the 8th-order controller, which is used to improve the four CCG modes. Accordingly, the control parameters of \mathbf{k}_p are varied in every $\Delta t = 1$ s, if the constraints in (14b) are not satisfied. The \mathbf{k}_p is compared with a generic controller, which is referred to as \mathbf{k}_c . The \mathbf{k}_c is designed by using objective function (14a) and (14b) with the same order as that of \mathbf{k}_p . The control parameters of \mathbf{k}_c are optimized at the normal operating point, i.e. using SI_i and SI_o during $t = [0 \ 1]$ s. However, the control parameters of \mathbf{k}_c are fixed as constant values until the end of simulation time.

Since this work considers effects of the CCG modes in which the frequencies are in the range of approximately 1.5 to 6 Hz, the observed time is set between 0.16 and 0.66 s to monitor the dynamic responses of these CCG modes. Typically, the state of charge of the BESS is normally observed from more than several minutes to hours [30]. Accordingly, the state of charge of the BESS can be neglected in this period.

Case Study 1: It is assumed that the loads are fluctuated between 1.5 and 4.5 MW in every 5 to 20 s. In real practice, a low-inertia microgrid such as a CIGRE microgrid benchmark [31] could experience randomly changing in loads over time. The timestamp of measurements is crucial to monitor the load variations. The lower the value of timestamp,

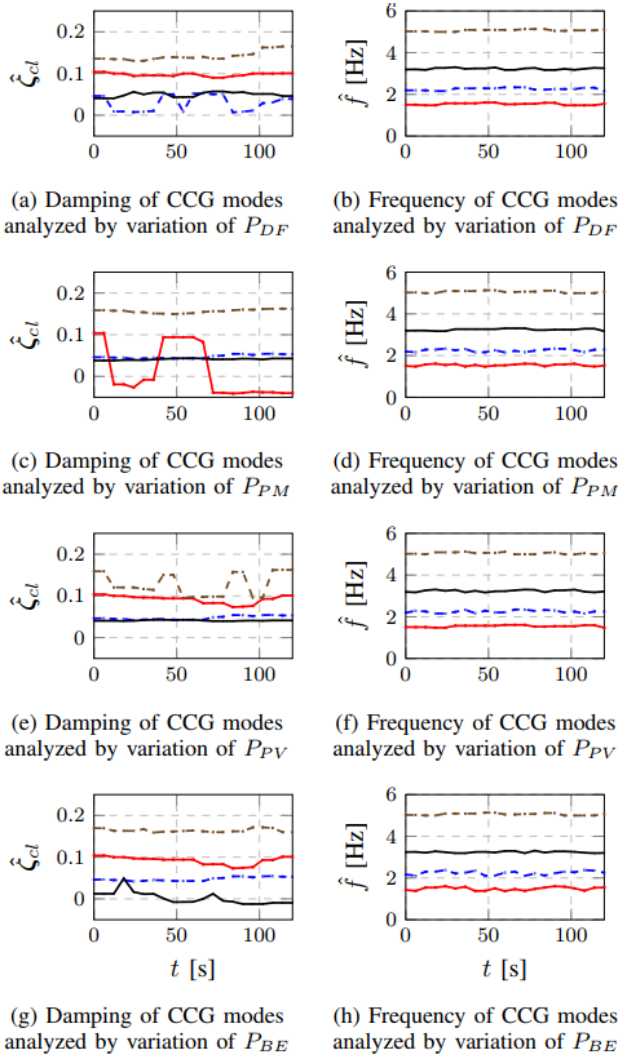


FIGURE 8. $\hat{\zeta}_{cl}$ and \hat{f} obtained from the CCG mode analysis; blue-dashed line: 1st CCG mode, red line: 2nd CCG mode, brown-dashed line: 3rd CCG mode, and black line: 4th CCG mode.

the more the detail of measuring load variations. The sampling rate of synchronized measurements can report the measured data between 10 and 30 samples in 1 s (or between 33 and 100 ms of timestamp) [32]. To make the microgrid conditions more sensitive to the CCG modes, the load variations at this rate are considered to verify performances of the proposed controller. Besides, the output powers of DFIG, PMSG, and SPV are managed by the active power controls in converters to meet these load demands. As a result, the total generation of such RESs is varied between 0.75 and 5 MW. Note that the DFIG and PMSG are operated according to the wind speed, which is associated to the variables ω_{DF} and ω_{PM} , while the SPV is operated according to the solar irradiation, which is related to the variable i_{PV} . Following on, the BESS is used to charge or discharge when the generation is greater or lower than the load demands, respectively. Consequently, Figs. 9 and 10 illustrate the transient response and the estimated damping of the CCG modes under such conditions, respectively.

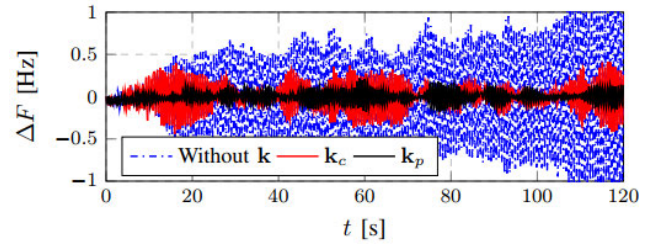


FIGURE 9. Response of ΔF in Case Study 1.

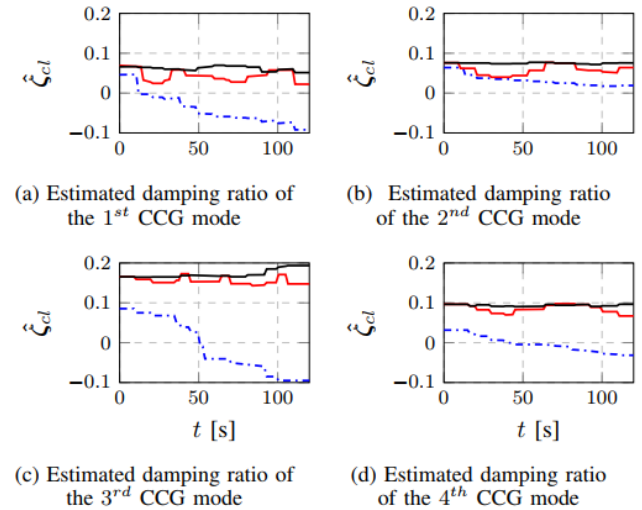


FIGURE 10. Estimated damping ratio in Case Study 1; blue-dashed line: Without \mathbf{k} , red line: \mathbf{k}_c , black line: \mathbf{k}_p .

Without \mathbf{k} , the ΔF amplitude gradually increases and the microgrid eventually becomes unstable. As can be observed, the $\hat{\zeta}_{cl}$ of the CCG modes moves to unstable region (negative value) under the changes in microgrid. After $t > 20$ s, the ΔF is not maintained within the acceptable range, i.e. $\Delta F \in [-0.3 \ 0.3]$ Hz. Therefore, this scenario highly requires the improvement of $\hat{\zeta}_{cl}$. It should be noted that, as reported by [33], there are no specific standards defined for the frequency limits of low-inertia and isolated microgrids since these microgrids highly depend on the mixed generations and loads. Therefore, the quick changes in the generations and loads in low-inertia microgrids may lead to large frequency deviations that are beyond standard limits. From a generator point-of-view, frequency standards such as the ISO 8528-5 standard [34] could be used to provide a guideline for the frequency limits. In this case, the frequency deviation, which is increased to 1 Hz in 120 s by the variations of generations and loads, is possible in the study low-inertia microgrid with CCGs.

On the other hand, with the optimal-fixed control parameters, the \mathbf{k}_c cannot keep the ΔF between -0.3 and 0.3 Hz. This implies that the $\hat{\zeta}_{cl}$ in the case of \mathbf{k}_c is sensitive to these changes. In comparison to the \mathbf{k}_p , the $\hat{\zeta}_{cl}$ is almost kept as constant values since the \mathbf{k}_p can adapt its control parameters to satisfy the constraints in (14b). As can be seen, the \mathbf{k}_p is robust to such microgrid changes. As a result, the \mathbf{k}_p

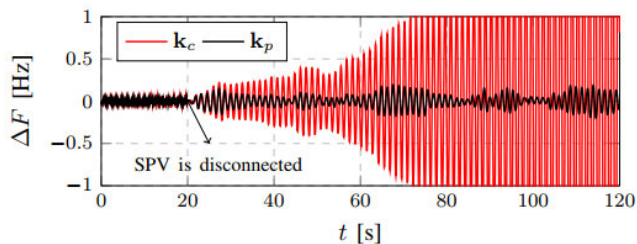


FIGURE 11. Response of ΔF in Case Study 2.

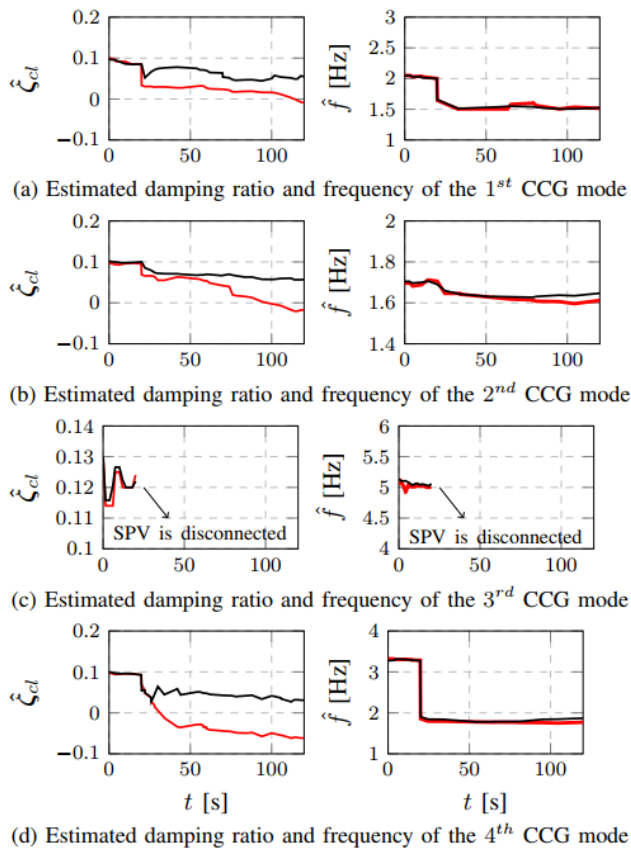


FIGURE 12. Estimated damping ratio and frequency in Case Study 2; red line: k_c , black line: k_p .

provides higher control performance resulting in the smaller ΔF amplitude.

Case Study 2: The total generation is identical to that of *Case Study 1*. It is assumed that the loads are altered between 0.5 and 6.5 MW in every 2 to 6 s. At $t = 20$ s, the SPV is disconnected from the microgrid. Accordingly, the BESS automatically manages the loads and outputs of the DFIG and PMSG. Fig. 11 shows the frequency deviation resulted by the k_c and k_p and Fig. 12 illustrates the estimated damping ratio and frequency of four CCG modes. During $t = [0 \ 20]$ s, before the disconnection of SPV, both controllers can suppress the frequency deviation. In addition, both k_c and k_p can significantly improve the damping ratios of the CCG modes. After the disconnection of SPV, the 3rd CCG mode belonging to the SPV disappears. As can be seen, all the estimated frequencies \hat{f} decrease to approximately 1.5 Hz resulting

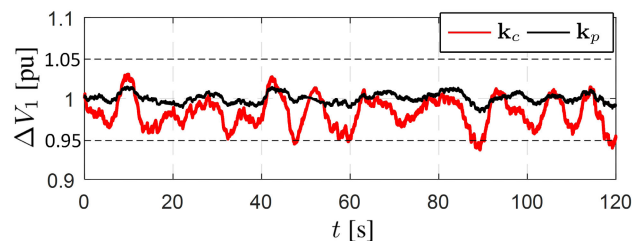


FIGURE 13. Response of ΔV_1 in Case Study 3.

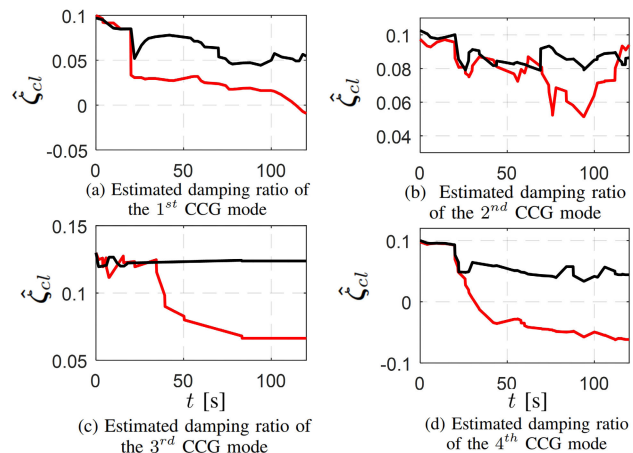


FIGURE 14. Estimated damping ratio and frequency in Case Study 3; red line: k_c , black line: k_p .

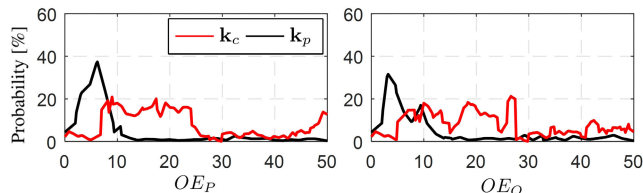


FIGURE 15. Probability analysis result of Case Study 4.

in the alteration of oscillation frequency in the microgrid. Moreover, most of $\hat{\zeta}_{cl}$ significantly drop to negative values, especially the 4th mode. After the change of microgrid topology, k_c with optimal-fixed control parameters cannot maintain the frequency deviation in the acceptable range, the ΔF severely fluctuates and eventually becomes unstable. By using k_p , the order of k_p is automatically changed to 6 (i.e. $p = q = 6$) to maintain the damping of the three CCG modes. Besides, all control parameters of k_p are optimally redesigned. Although the microgrid topology changes, $\hat{\zeta}_{cl}$ of the three CCG modes are maintained around 5% resulting in the smaller fluctuation of ΔF . Obviously, the k_p can keep the frequency deviation within the acceptable range and it is robust to the disconnection of CCG.

Case Study 3: It is assumed that the reactive powers of loads are varied between 0.05 and 1.5 MVAR in every 5 to 10 s. To demonstrate the controller performance in terms of reactive power variations, the proposed controller k_p can be modified as follows: inputs of the 4SID are changed by

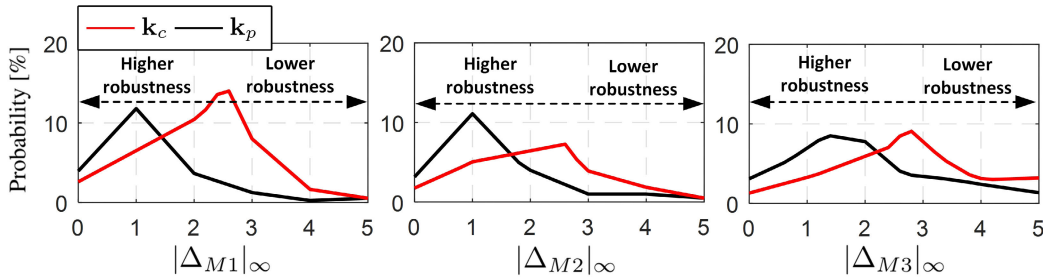


FIGURE 16. Probability analysis result of Case Study 5.

$SI_i = \Delta \bar{Q}$ and $SI_o = \Delta V_1$ while the objective function (14a), and constraints (14b) and (14c) remain the same for the adaptive robust controller design. Fig. 13 shows the voltage variation of bus 1. In comparison, the fluctuation of voltage in the case of \mathbf{k}_p is relatively small. On the other hand, the controller \mathbf{k}_c cannot resist the reactive power variations of loads, the voltage of bus 1 is not in the acceptable range, i.e between 0.95 and 1.05 pu. Fig. 14 illustrates the estimated damping ratios of CCG modes. It can be seen that the damping ratios in the case of \mathbf{k}_c are significantly degraded, especially in the 4th CCG mode. Conversely, the variations of reactive power slightly affect the performance of controller \mathbf{k}_p , the damping ratios of all CCG modes are more than 0.05 or 5%.

With the modification in the 4SID, the result in this case guarantees that the proposed control algorithm can also deal with the reactive power variations of loads.

Case Study 4: In this case, the observation errors in the input and output signals of \mathbf{k}_c and \mathbf{k}_p are evaluated by using the sensitivity analysis. Possible scenarios are considered as follows:

- 1) For the observation error in the case of active power variations, the input of controller is the mean active power deviation of all CCGs and loads, i.e. $\Delta y_{CO} = \Delta \bar{P}$, while the output of controller is sent to four CCGs (see Figs. 1 and 2). It is assumed that one or more signal(s) of input Δy_{CO} is/are missing (i.e. ΔP_{DF} or/and ΔP_{PM} or/and ΔP_{PV} or/and ΔP_{BE} or/and ΔP_L). At the same time, it is also assumed that the controller fails to send the output to any CCGs. As a result, the total combination of these scenarios is equal to $2^9 = 512$.
- 2) For the observation error in the case of reactive power variations, all conditions are the same as that of step 1) except $\Delta y_{CO} = \Delta \bar{Q}$, this also results in the same total combination of possible scenarios ($2^9 = 512$).
- 3) The microgrid operating points in *Case Study 1* and *Case Study 3* are respectively used to evaluate the performances of both \mathbf{k}_c and \mathbf{k}_p in steps 1) and 2). In this paper, the following equations are devised to justify the observation error for each scenario as,

$$OE_P = \left| \int_{t=0}^{t_{sim}} |\Delta F_w| dt - \int_{t=0}^{t_{sim}} |\Delta F| dt \right|, \quad (15a)$$

$$OE_Q = \left| \int_{t=0}^{t_{sim}} |\Delta V_{1,w}| dt - \int_{t=0}^{t_{sim}} |\Delta V_1| dt \right|, \quad (15b)$$

where OE_P and OE_Q are respectively the observation errors used for steps 1) and 2), t_{sim} is the total simulation time, and ΔF_w and $\Delta V_{1,w}$ are the signals ΔF and ΔV_1 without the observation errors (or ΔF and ΔV_1 obtained from *Case Study 1* and *Case Study 3*).

In (15a) and (15b), the lower the values of OE_P and OE_Q , the lower the effects of observation error on controller performance. After conducting steps 1) to 3), the results from (15a) and (15b) are collected to conduct the probability analysis. Accordingly, Fig. 15 shows the percentage of OE_P and OE_Q in the cases of \mathbf{k}_c and \mathbf{k}_p . In the case of \mathbf{k}_c , the value of OE_P is varied between 7 and 24.5 with the probability around 16%, and between 42 and 50 with the probability between 3.5 and 15%. On the other hand, in the case of \mathbf{k}_p , the value of OE_P falls within the range of 2 to 12 with the highest probability of 39.8%. The same trend also occurs with the value of OE_Q . According to (15a) and (15b), this implies that the controller \mathbf{k}_p provides better control performances under the impacts of observation errors.

Case Study 5: In this case, the robustness of controllers is investigated by varying the converter controller gains. The simulation setup is given as follows:

- 1) All gains of the proportional-integral (known as PI) controllers in CCG converter control loops (see Fig. 2) are randomly varied from 0.1 to 10 pu while the generations and loads are randomly changed by $\pm 20\%$ from *Case Study 1*.
- 2) Consequently, the ∞ -norms of three sensitivity functions, i.e. $|\Delta M_1|_\infty$, $|\Delta M_2|_\infty$, and $|\Delta M_3|_\infty$, are calculated to evaluate the robustness of the controllers \mathbf{k}_c and \mathbf{k}_p against such variations.
- 3) Repeat the steps 1) and 2) for 1,000 scenarios to conduct the probability analysis.

Fig. 16 shows the probability analysis of controller robustness under various microgrid operating points. Having in mind that the lower the values of $|\Delta M_1|_\infty$, $|\Delta M_2|_\infty$, and $|\Delta M_3|_\infty$, the higher the robustness against microgrid uncertainties. In the case of \mathbf{k}_p , the occurrences of smaller values of $|\Delta M_1|_\infty$, $|\Delta M_2|_\infty$, and $|\Delta M_3|_\infty$ are higher than those of the controller \mathbf{k}_c . It implies that the controller \mathbf{k}_p is more robust than the controller \mathbf{k}_c under various microgrid operating points and converter controller gains.

V. CONCLUSION

This paper presents the adaptive robust control using the signal identification of a low-inertia microgrid. The CCG modes are taken into account in the controller design process. Following on, the sensitivity functions are considered for the robustness of controller along with microgrid changes. The proposed method is more practical in actual microgrids since it does not require any exact microgrid parameters to analyze the CCG modes and design the controller. Besides, the accuracy of estimated microgrid model is very high while the order of the obtained controller is much smaller than that of the original model. As verified in the simulation results, the CCG modes are shown to be detrimental to a low-inertia microgrid. The proposed controller can be designed by identifying the signals of load patterns, output of CCGs, and frequency deviation. The proposed controller also provides a better performance than that of a conventional optimal-fixed controller under various changes in RES outputs and loads. Salient features of the proposed control are expected for future microgrids with 100% penetration of CCGs.

APPENDIX

A. DIFFERENTIAL EQUATIONS OF DFIG, PMSG, SPV, AND BESS

The differential equations of DFIG, PMSG, SPV, and BESS are given as follows:

For the DFIG model:

$$\dot{\omega}_{DF}(t) = \frac{1}{2H_{DF}} \left(-\frac{P_{m,DF}(t)}{\omega_{DF}(t)} - \Gamma_{e,DF}(t) \right), \quad (\text{A-1a})$$

$$\begin{bmatrix} \dot{i}_{DF}^{d,ro}(t) \\ \dot{i}_{DF}^{q,ro}(t) \\ \dot{i}_{DF}^{d,gr}(t) \\ \dot{i}_{DF}^{q,gr}(t) \end{bmatrix} = -M_{1,DF} M_{2,DF} \begin{bmatrix} i_{DF}^{d,ro}(t) \\ i_{DF}^{q,ro}(t) \\ i_{DF}^{d,gr}(t) \\ i_{DF}^{q,gr}(t) \end{bmatrix} + M_{1,DF}^{-1} \begin{bmatrix} v_{DF}^{d,ro}(t) \\ v_{DF}^{q,ro}(t) \\ v_{DF}^{d,gr}(t) \\ v_{DF}^{q,gr}(t) \end{bmatrix}, \quad (\text{A-1b})$$

$$M_{1,DF} = \begin{bmatrix} L_{DF}^s & 0 & L_{DF}^m & 0 \\ 0 & L_{DF}^s & 0 & L_{DF}^m \\ L_{DF}^m & 0 & L_{DF}^r & 0 \\ 0 & L_{DF}^m & 0 & L_{DF}^r \end{bmatrix}, \quad (\text{A-1c})$$

$$M_{2,DF} = \begin{bmatrix} R_{DF}^s & L_{DF}^s & 0 & L_{DF}^m \\ -L_{DF}^s & R_{DF}^s & -L_{DF}^m & 0 \\ 0 & \frac{1-\omega_{DF}(t)}{L_{DF}^m} & R_{DF}^r & \frac{1-\omega_{DF}(t)}{L_{DF}^r} \\ -\frac{1-\omega_{DF}(t)}{L_{DF}^m} & 0 & -\frac{1-\omega_{DF}(t)}{L_{DF}^r} & 0 \end{bmatrix}, \quad (\text{A-1d})$$

$$\dot{v}_{DF}^{dc}(t) = \frac{3}{2C_{DF}^{dc} v_{DF}^{dc}(t)} \left(v_{DF}^{d,gr}(t) i_{DF}^{d,gr}(t) + v_{DF}^{q,gr}(t) i_{DF}^{q,gr}(t) - v_{DF}^{d,ro}(t) i_{DF}^{d,ro}(t) - v_{DF}^{q,ro}(t) i_{DF}^{q,ro}(t) \right), \quad (\text{A-1e})$$

$$\dot{\theta}_{DF}(t) = \frac{-\theta_{DF}(t)}{T_{\theta,DF}} - \frac{K_{\theta,DF}}{T_{\theta,DF}} (\omega_{DF}(t) - 1), \quad (\text{A-1f})$$

For the PMSG model:

$$\dot{\omega}_{PM}(t) = \frac{1}{2H_{PM}} \left(-\frac{P_{m,PM}(t)}{\omega_{PM}(t)} - \Gamma_{e,PM}(t) \right), \quad (\text{A-2a})$$

$$\begin{bmatrix} \dot{i}_{PM}^{d,ro}(t) \\ \dot{i}_{PM}^{q,ro}(t) \\ \dot{i}_{PM}^{d,ge}(t) \\ \dot{i}_{PM}^{q,ge}(t) \end{bmatrix} = -M_{1,PM} M_{2,PM} \begin{bmatrix} i_{PM}^{d,ro}(t) \\ i_{PM}^{q,ro}(t) \\ i_{PM}^{d,ge}(t) \\ i_{PM}^{q,ge}(t) \end{bmatrix} + M_{1,PM}^{-1} \begin{bmatrix} v_{PM}^{d,ro}(t) \\ v_{PM}^{q,ro}(t) \\ v_{PM}^{d,ge}(t) \\ v_{PM}^{q,ge}(t) \end{bmatrix}, \quad (\text{A-2b})$$

$$M_{1,PM} = \begin{bmatrix} L_{PM}^s & 0 & L_{PM}^m & 0 \\ 0 & L_{PM}^s & 0 & L_{PM}^m \\ L_{PM}^m & 0 & L_{PM}^r & 0 \\ 0 & L_{PM}^m & 0 & L_{PM}^r \end{bmatrix}, \quad (\text{A-2c})$$

$$M_{2,PM} = \begin{bmatrix} R_{PM}^s & L_{PM}^s & 0 & L_{PM}^m \\ -L_{PM}^s & R_{PM}^s & -L_{PM}^m & 0 \\ 0 & \frac{\omega_{PM}(t)}{L_{PM}^m} & R_{PM}^r & \frac{\omega_{PM}(t)}{L_{PM}^r} \\ -\frac{\omega_{PM}(t)}{L_{PM}^m} & 0 & -\frac{\omega_{PM}(t)}{L_{PM}^r} & 0 \end{bmatrix}, \quad (\text{A-2d})$$

$$rCl v_{PM}^{dc}(t) = \frac{3}{2C_{PM}^{dc} v_{PM}^{dc}(t)} \left(v_{PM}^{d,ge}(t) i_{PM}^{d,ge}(t) + v_{PM}^{q,ge}(t) i_{PM}^{q,ge}(t) - v_{PM}^{d,gr}(t) i_{PM}^{d,gr}(t) - v_{PM}^{q,gr}(t) i_{PM}^{q,gr}(t) \right), \quad (\text{A-2e})$$

$$\dot{\theta}_{PM}(t) = \frac{-\theta_{PM}(t)}{T_{\theta,PM}} - \frac{K_{\theta,PM}}{T_{\theta,PM}} (\omega_{PM}(t) - 1), \quad (\text{A-2f})$$

For the SPV model:

$$\dot{i}_{PV}(t) = \frac{d \left(i_{ph}(t, \gamma_s(t)) - i_0 e^{f(v_{PV}(t), Temp(t))} \right)}{dt}, \quad (\text{A-3a})$$

$$\dot{i}_{PV}(t) = \frac{-R_{PV} i_{PV}(t)}{L_{PV}} + \frac{v_{PV}(t)}{L_{PV}}, \quad (\text{A-3b})$$

$$\dot{v}_{PV}^{dc}(t) = \frac{3i_{PV}^{dc}(t)}{2C_{PV}^{dc} v_{PV}^{dc}(t)}, \quad (\text{A-3c})$$

$$\dot{i}_{PV}^{d,gr}(t) = \frac{v_{PV}^{d,gr}(t)}{L_{PV}} + \frac{R_{PV}^{gr} i_{PV}^{d,gr}(t)}{L_{PV}}, \quad (\text{A-3d})$$

$$\dot{i}_{PV}^{q,gr}(t) = \frac{v_{PV}^{q,gr}(t)}{L_{PV}} + \frac{R_{PV}^{gr} i_{PV}^{q,gr}(t)}{L_{PV}}, \quad (\text{A-3e})$$

$$\dot{v}_{PV}^{d,gr}(t) = \frac{v_{PV}^{d,gr}(t)}{C_{PV}} - \frac{R_{PV}^{gr} i_{PV}^{q,gr}(t)}{C_{PV}}, \quad (\text{A-3f})$$

$$\dot{v}_{PV}^{q,gr}(t) = \frac{v_{PV}^{q,gr}(t)}{C_{PV}} - \frac{R_{PV}^{gr} i_{PV}^{d,gr}(t)}{C_{PV}}, \quad (\text{A-3g})$$

For the BESS model:

$$\dot{v}_{BE}^{dc}(t) = \frac{3i_{BE}^{dc}(t)}{2C_{BE}^{dc} v_{BE}^{dc}(t)}, \quad (\text{A-4a})$$

$$\dot{i}_{BE}^d(t) = \frac{v_{BE}^d(t)}{L_{BE}} + \frac{R_{BE} i_{BE}^d(t)}{L_{BE}}, \quad (\text{A-4b})$$

$$\dot{i}_{BE}^q(t) = \frac{v_{BE}^q(t)}{L_{BE}} + \frac{R_{BE} i_{BE}^q(t)}{L_{BE}}, \quad (\text{A-4c})$$

$$\dot{v}_{BE}^d(t) = \frac{v_{BE}^d(t)}{C_{BE}} - \frac{RPV i_{BE}^q(t)}{C_{BE}}, \quad (A-4d)$$

$$\dot{i}_{BE}^q(t) = \frac{v_{BE}^q(t)}{C_{BE}} - \frac{RPV i_{BE}^d(t)}{C_{BE}}, \quad (A-4e)$$

where superscript m represents the mutual inductance, R , L , and C are respectively resistance, inductance and capacitance, H is the aggregate generator inertia, Γ_e is the electrical rotor torque, and K_θ and T_θ are the pitch angle gain and control time constant, i_{ph} and i_0 are respectively the current produced by solar irradiation (γ_s) and saturation current, and $Temp$ is the temperature at SPV arrays.

B. COMPUTATION OF SYSTEM MATRICES USING 4SID

The computation of state matrices \hat{A} , \hat{B} , \hat{C} , and \hat{D} is given by the following steps [25],

- 1) Equally partition the measured signals SI_i and SI_o . For example, $SI_{i,r} = [SI_{i,1}, \dots, SI_{i,n_r}]$ and $SI_{o,r} = [SI_{o,1}, \dots, SI_{o,n_r}]$.

- 2) Let define the oblique projection \mathcal{O} as,

$$\begin{aligned} \mathcal{O}_{r-1} &\stackrel{\text{def}}{=} SI_{o,r-1}/SI_{i,r-1} \mathbf{H}_{r+1}, \\ &= \Theta_{r-1} \hat{\mathbf{x}}_{r+1}, \end{aligned} \quad (A-5)$$

where \mathbf{H} is the Hankel matrix containing the past inputs and outputs, $\hat{\mathbf{x}}$ is the estimated state matrix, and Θ is the extended observability matrix.

- 3) Calculate the oblique projections at patterns r and $r-1$ by: $\mathcal{O}_r = SI_{o,r}/SI_{i,r} \mathbf{H}_r$, and \mathcal{O}_{r-1} in (A-5).
- 4) Calculate the singular value decomposition (known as *SVD*) and determine the estimated model order by inspecting the singular values in $S_r = \begin{bmatrix} S_{11,r} & 0 \\ 0 & 0 \end{bmatrix}$. Next, partition the *SVD* to obtain $U_{1,r}$ and $S_{11,r}$ by,

$$\begin{aligned} W_{1,r} \mathcal{O}_r W_{2,r} &= [U_{1,r} \ U_{2,r}] \begin{bmatrix} S_{11,r} & 0 \\ 0 & 0 \end{bmatrix} \begin{bmatrix} V_{1,r}^\top \\ V_{2,r}^\top \end{bmatrix} \\ &= U_{1,r} S_{11,r} V_{2,r}^\top \end{aligned} \quad (A-6)$$

where $W_1 = [U_1 \ U_2]$ and $W_2 = [V_1^\top \ V_2^\top]^\top$ are the weighting matrices.

- 5) Determine Θ_r and Θ_{r-1} as,

$$\Theta_r = W_{1,r}^{-1} U_{1,r} \sqrt{S_{11,r}}, \quad (A-7a)$$

$$\Theta_{r-1} = \underline{\Theta}_r, \quad (A-7b)$$

where $\underline{\Theta}_r$ means the matrix Θ_r without the last row.

- 6) The state sequences $\hat{\mathbf{x}}_r$ and $\hat{\mathbf{x}}_{r+1}$ are calculated by,

$$\hat{\mathbf{x}}_r = \Theta_r^\perp \mathcal{O}_r, \quad (A-8a)$$

$$\hat{\mathbf{x}}_{r+1} = \underline{\Theta}_r^\perp \mathcal{O}_{r-1}, \quad (A-8b)$$

where superscript \perp means the orthogonal complement.

- 7) Solve the set of estimated state matrices \hat{A} , \hat{B} , \hat{C} , and \hat{D} by,

$$\begin{bmatrix} \hat{\mathbf{x}}_{r+1} \\ SI_{o,r|r} \end{bmatrix} = \begin{bmatrix} \hat{A}_r & \hat{B}_r \\ \hat{C}_r & \hat{D}_r \end{bmatrix} \begin{bmatrix} \hat{\mathbf{x}}_r \\ SI_{i,r|r} \end{bmatrix}, \quad (A-9)$$

where $SI_{i,r|r}$ and $SI_{o,r|r}$ are the specified values of SI_i and SI_o at any sequence r , respectively. Note that these set of matrices can be solved by a linear least squares method.

- 8) Repeat the steps 1) to 7) for $r = 1, \dots, n_r$. We get $[\hat{A}_1, \dots, \hat{A}_{n_r}]$, $[\hat{B}_1, \dots, \hat{B}_{n_r}]$, $[\hat{C}_1, \dots, \hat{C}_{n_r}]$, and $[\hat{D}_1, \dots, \hat{D}_{n_r}]$. Accordingly, the stability indices can be obtained in every moving windows to design the controller.

C. ANALYSIS OF SYSTEM ROBUSTNESS

Fig. 17 illustrates a typical closed-loop system configuration with uncertainties [29], where \mathbf{d} , \mathbf{n} , and \mathbf{r} are the sets of disturbances, communication uncertainties, and references, respectively. The following relationships can be obtained as,

$$\begin{aligned} \mathbf{y} &= (I + \hat{G}\mathbf{k})^{-1} \hat{G}\mathbf{k} \cdot \mathbf{r} + (I + \hat{G}\mathbf{k})^{-1} \cdot \mathbf{d} \\ &\quad - (I + \hat{G}\mathbf{k})^{-1} \hat{G}\mathbf{k} \cdot \mathbf{n}, \end{aligned} \quad (A-10a)$$

$$\begin{aligned} \Delta \mathbf{u}^\tau &= \mathbf{k} (I + \hat{G}\mathbf{k})^{-1} \cdot \mathbf{r} - \mathbf{k} (I + \hat{G}\mathbf{k})^{-1} \cdot \mathbf{d} \\ &\quad - \mathbf{k} (I + \hat{G}\mathbf{k})^{-1} \cdot \mathbf{n}. \end{aligned} \quad (A-10b)$$

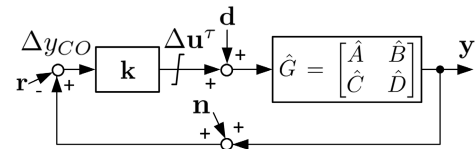


FIGURE 17. A typical closed-loop configuration of \mathbf{k} , \hat{G} , and uncertainties.

It is known in Section III-B that we have defined the sensitivity functions $\Delta_{M1} = (I + \hat{G}\mathbf{k})^{-1}$, $\Delta_{M2} = -(I + \hat{G}\mathbf{k})^{-1} \hat{G}\mathbf{k}$, and $\Delta_{M3} = \mathbf{k} (I + \hat{G}\mathbf{k})^{-1}$. Substituting Δ_{M1} , Δ_{M2} , and Δ_{M3} into (A-10a) and (A-10b) yields,

$$\mathbf{y} = -\Delta_{M2} \cdot \mathbf{r} + \Delta_{M1} \cdot \mathbf{d} + \Delta_{M2} \cdot \mathbf{n}, \quad (A-11a)$$

$$\Delta \mathbf{u}^\tau = \Delta_{M3} \cdot \mathbf{r} - \Delta_{M3} \cdot \mathbf{d} - \Delta_{M3} \cdot \mathbf{n}. \quad (A-11b)$$

It can be observed in (A-11a) and (A-11b) that the sensitivity functions Δ_{M1} , Δ_{M2} , and Δ_{M3} are known and these terms are the factors of \mathbf{r} , \mathbf{d} , and \mathbf{n} . In this paper, the control parameters of \mathbf{k} are optimally changed to minimize the ∞ -norms of Δ_{M1} , Δ_{M2} , and Δ_{M3} . Consequently, the disturbance attenuation, communication uncertainty rejection, and good control performance can be attended in both input and output sides of the controller \mathbf{k} .

D. MICROGRID PARAMETERS

In this paper, the parameters of DFIG are provided as follows: DFIG size = 1.5 MW, DFIG converter rate = 25% of DFIG size, $H_{DF} = 0.15$ GVAs, $R_{DF}^r = 0.2 \ \Omega$, $R_{DF}^s = 0.05 \ \Omega$, $L_{DF}^m = L_{DF}^s = 0.265$ mH, $L_{DF}^r = 0.065$ mH, and $C_{DF}^{dc} = 0.54$ mF. The parameters of PMSG are provided as follows: PMSG size = 1.5 MW, PMSG converter rate = 25% of PMSG size (1.5 MW), $H_{PM} = 0.12$ GVAs, $R_{PM}^s = 0.15 \ \Omega$,

$R_{PM}^r = 0.01 \Omega$, $L_{PM}^m = L_{PM}^s = 0.125$ mH, $L_{PM}^r = 0.05$ mH, and $C_{PM}^{dc} = 0.54$ mF. The parameters of SPV are provided as follows: SPV size = 1 MW, SPV converter rate = 20% of SPV size (1 MW), $R_{PV} = 0.1 \Omega$, $L_{PV} = 0.025$ mH, $C_{PV}^{dc} = 0.45$ mF, $R_{PV}^{gr} = 0.02 \Omega$, $L_{PV}^{gr} = 0.0125$ mH, and $C_{PV} = 0.001$ mF. The parameters of BESS are given as follows: BESS size = 1 MW, BESS converter rate = 25% of SPV size (1 MW), $C_{BE}^{dc} = 0.65$ mF, $R_{BE} = 0.02 \Omega$, $L_{BE} = 0.0125$ mH, and $C_{BE} = 0.001$ mF.

REFERENCES

- [1] T. Kerdphol, F. S. Rahman, M. Watanabe, and Y. Mitani, "Robust virtual inertia control of a low inertia microgrid considering frequency measurement effects," *IEEE Access*, vol. 7, pp. 57550–57560, 2019.
- [2] K. S. Ratnam, K. Palanisamy, and G. Yang, "Future low-inertia power systems: Requirements, issues, and solutions—A review," *Renew. Sustain. Energy Rev.*, vol. 124, May 2020, Art. no. 109773.
- [3] Z. Wang, B. Chen, J. Wang, and J. Kim, "Decentralized energy management system for networked microgrids in grid-connected and islanded modes," *IEEE Trans. Smart Grid*, vol. 7, no. 2, pp. 1097–1105, Mar. 2015.
- [4] X. Li, Z. Li, L. Guo, J. Zhu, Y. Wang, and C. Wang, "Enhanced dynamic stability control for low-inertia hybrid AC/DC microgrid with distributed energy storage systems," *IEEE Access*, vol. 7, pp. 91234–91242, 2019.
- [5] F. K. Tuffner, K. P. Schneider, J. Hansen, and M. A. Elizondo, "Modeling load dynamics to support resiliency-based operations in low-inertia microgrids," *IEEE Trans. Smart Grid*, vol. 10, no. 3, pp. 2726–2737, May 2019.
- [6] D. Gautam, V. Vittal, and T. Harbour, "Impact of increased penetration of DFIG-based wind turbine generators on transient and small signal stability of power systems," *IEEE Trans. Power Syst.*, vol. 24, no. 3, pp. 1426–1434, Aug. 2009.
- [7] Y. Yoldaş, A. Önen, S. M. Mueeen, A. V. Vasilakos, and İ. Alan, "Enhancing smart grid with microgrids: Challenges and opportunities," *Renew. Sustain. Energy Rev.*, vol. 72, pp. 205–214, May 2017.
- [8] F. Guo, C. Wen, J. Mao, and Y. D. Song, "Distributed secondary voltage and frequency restoration control of droop-controlled inverter-based microgrids," *IEEE Trans. Ind. Electron.*, vol. 62, no. 7, pp. 4355–4364, Jul. 2014.
- [9] J. Chen, M. Liu, F. Milano, and T. O'Donnell, "100% converter-interfaced generation using virtual synchronous generator control: A case study based on the Irish system," *Electr. Power Syst. Res.*, vol. 187, Oct. 2020, Art. no. 106475.
- [10] R. Dong, S. Liu, G. Liang, X. An, and Y. Xu, "Output control method of microgrid VSI control network based on dynamic matrix control algorithm," *IEEE Access*, vol. 7, pp. 158459–158480, 2019.
- [11] C. X. Rosero, M. Velasco, P. Martí, A. Camacho, J. Miret, and M. Castilla, "Active power sharing and frequency regulation in droop-free control for islanded microgrids under electrical and communication failures," *IEEE Trans. Ind. Electron.*, vol. 67, no. 8, pp. 6461–6472, Aug. 2020.
- [12] K. S. Rajesh, S. S. Dash, R. Rajagopal, and R. Sridhar, "A review on control of ac microgrid," *Renew. Sustain. Energy Rev.*, vol. 71, no. 1, pp. 814–819, 2017.
- [13] M. Hossain, H. Pota, and W. Issa, "Overview of AC microgrid controls with inverter-interfaced generations," *Energies*, vol. 10, no. 9, p. 1300, 2017.
- [14] B. Long, Y. Liao, K. T. Chong, J. Rodriguez, and J. M. Guerrero, "MPC-controlled virtual synchronous generator to enhance frequency and voltage dynamic performance in islanded microgrids," *IEEE Trans. Smart Grid*, vol. 12, no. 2, pp. 953–964, Mar. 2021.
- [15] M. Nasr, A. Rabiee, and I. Kamwa, "MPC and robustness optimisation-based EMS for microgrids with high penetration of intermittent renewable energy," *IET Gener., Transmiss. Distrib.*, vol. 14, no. 22, pp. 5239–5248, Nov. 2020.
- [16] A. Abazari, M. M. Soleymani, M. Babaei, M. Ghafouri, H. Monsef, and M. T. H. Beheshti, "High penetrated renewable energy sources-based AOMPC for microgrid's frequency regulation during weather changes, time-varying parameters and generation unit collapse," *IET Gener., Transmiss. Distrib.*, vol. 14, no. 22, pp. 5164–5182, Nov. 2020.
- [17] J. Hu, Y. Shan, J. M. Guerrero, A. Ioinovici, K. W. Chan, and J. Rodriguez, "Model predictive control of microgrids—An overview," *Renew. Sustain. Energy Rev.*, vol. 136, Feb. 2021, Art. no. 110422.
- [18] W. R. Tarnate, L. T. Upb, S. K. Gurumurthy, and A. Musa, "No 727481 RESERVE D1. 2 requirements placed on energy systems on transition to 100% RES," Inst. Automat. Complex Power Syst., U.K., Tech. Rep., 2017.
- [19] B. Lu and B. T. Ooi, "Nonlinear control of voltage-source converter systems," *IEEE Trans. Power Electron.*, vol. 22, no. 4, pp. 1186–1195, Jul. 2007.
- [20] A. M. Khalil and R. Iravani, "Power system coherency identification under high depth of penetration of wind power," *IEEE Trans. Power Syst.*, vol. 33, no. 5, pp. 5401–5409, Sep. 2018.
- [21] H.-W. Kim, S.-S. Kim, and H.-S. Ko, "Modeling and control of PMSG-based variable-speed wind turbine," *Electr. Power Syst. Res.*, vol. 80, no. 1, pp. 46–52, Jan. 2010.
- [22] S. Adhikari and F. Li, "Coordinated V-f and P-Q control of solar photovoltaic generators with MPPT and battery storage in microgrids," *IEEE Trans. Smart Grid*, vol. 5, no. 3, pp. 1270–1281, May 2014.
- [23] M. Döhler and L. Mevel, "Fast multi-order computation of system matrices in subspace-based system identification," *Control Eng. Pract.*, vol. 20, no. 9, pp. 882–894, Sep. 2012.
- [24] L. Ljung, *System Identification Toolbox 7: Getting Started Guide*. Portola Valley, CA, USA: MathWorks, 2008.
- [25] B. De Moor, P. Van Overschee, and W. Favoreel, "Algorithms for subspace state-space system identification: An overview," in *Applied and Computational Control, Signals, and Circuits*. Boston, MA, USA: Birkhäuser, 1999, pp. 247–311.
- [26] S. Skoqestad and I. Postlethwaite, *Multiple Feedback Control: Analysis and Design*, 2nd ed. Hoboken, NJ, USA: Wiley, 2005.
- [27] B. Erkus and Y. Lee, "Linear matrix inequalities and MATLAB LMI toolbox," Univ. Southern California Group Meeting Rep., Los Angeles, CA, USA, Tech. Rep., 2004.
- [28] G. Balas, R. Chiang, A. Packard, and M. Safonov, "Robust control toolbox user's guide," Math Works, Portola Valley, CA, USA, Tech. Rep., 2007.
- [29] D.-W. Gu, P. Petkov, and M. M. Konstantinov, *Robust Control Design With MATLAB*, 2nd ed. Springer, 2005.
- [30] Y. Hua, X. Shentu, Q. Xie, and Y. Ding, "Voltage/frequency deviations control via distributed battery energy storage system considering state of charge," *Appl. Sci.*, vol. 9, no. 6, p. 1148, 2019.
- [31] B. V. Solanki, A. Raghurajan, K. Bhattacharya, and C. A. Cañizare, "Including smart loads for optimal demand response in integrated energy management systems for isolated microgrids," *IEEE Trans. Smart Grid*, vol. 8, no. 4, pp. 1739–1748, Jul. 2015.
- [32] W. Meng, X. Wang, Z. Wang, and I. Kamwa, "Impact of causality on performance of phasor measurement unit algorithms," *IEEE Trans. Power Syst.*, vol. 33, no. 2, pp. 1555–1565, Mar. 2017.
- [33] U. Tamrakar, D. Shrestha, M. Maharjan, B. P. Bhattarai, T. M. Hansen, and R. Tonkoski, "Virtual inertia: Current trends and future directions," *Appl. Sci.*, vol. 7, no. 7, p. 654, 2017.
- [34] *Reciprocating Internal Combustion Engine Driven Alternating Current Generating Sets Part 5: Generating Sets*, Standard ISO 8528-5:2018, Sep. 2020. [Online]. Available: <https://www.iso.org/standard/711009.html>



ISSARACHAI NGAMROO (Senior Member, IEEE) received the Ph.D. degree in electrical engineering from Osaka University, Osaka, Japan, in 2000. He is currently a Professor with the Department of Electrical Engineering, Faculty of Engineering, King Mongkut's Institute of Technology Ladkrabang, Bangkok, Thailand. His research interests include power system stability, dynamic, and control.



TOSSAPORN SURINKAEW received the B.Eng. and M.Eng. degrees in electrical engineering from King Mongkut's Institute of Technology Ladkrabang, Bangkok, Thailand, in 2012 and 2014, respectively. He is currently pursuing the Ph.D. degree with Central Queensland University, Australia. His research interests include power system modeling, computation, and control.